



Visible-light-active Rh-doped SrTiO₃: Effect of Rh doping on the structural characteristics contributing to outstanding photocatalytic activity

Tamás Gyulavári^{a,*}, Fanni Bóka^a, Milica Todea^{b,c}, Áron Ágoston^{a,d}, Ákos Kukovecz^a, Zoltán Kónya^a, Zsolt Pap^{a,b,e,**}

^a Department of Applied and Environmental Chemistry, University of Szeged, Rerrich Béla Sqr. 1, Szeged 6720, Hungary

^b Nanostructured Materials and Bio-Nano-Interfaces Center, Interdisciplinary Research Institute on Bio-Nano-Sciences, Babeş-Bolyai University, T. Laurian 42, Cluj-Napoca 400271, Romania

^c Faculty of Medicine, Iuliu Hațieganu University of Medicine and Pharmacy, Victor Babeş 8, Cluj-Napoca 400012, Romania

^d Department of Physical Chemistry and Materials Sciences, University of Szeged, Aradi v. Sqr. 1, 6720 Szeged, Aradi v. Sqr. 1, Szeged 6720, Hungary

^e Centre for 3B, Babeş-Bolyai University, Clinicilor 5–7, Cluj-Napoca 400006, Romania

ARTICLE INFO

Keywords:

Photocatalysis
Strontium titanate
Rhodium
Doping
Visible light
Phenol

ABSTRACT

Strontium titanate photocatalysts were doped with rhodium (0, 1, 5, 10, and 15 at%) via a hydrothermal method to enhance their visible light absorbance. The samples were characterized by X-ray diffractometry, X-ray photoelectron spectroscopy, infrared spectroscopy, nitrogen adsorption, scanning and transmission electron microscopy, diffuse reflectance spectroscopy, and photoluminescence measurements. Their photocatalytic activity was evaluated by the photocatalytic oxidation of phenol under visible light irradiation, using the non-Rh-containing sample as a reference. All the applied rhodium was successfully incorporated into the cubic crystal lattice. Rhodium doping resulted in significantly enhanced visible light absorption and suppressed charge recombination. The photocatalytic activity was enhanced to an exceptionally large degree: the best sample completely degraded phenol in 1 h under visible light. The optimal rhodium amount was found to be 5 at%. The high photocatalytic activity was attributed to the resultant effect of enhanced visible light absorbance, suppressed charge recombination, and high Rh³⁺/Rh⁴⁺ ratio.

1. Introduction

Strontium titanate (SrTiO₃) photocatalysts have received significant attention due to their high photoactivity, low cost, negligible toxicity, and high stability [1,2]. Quantum yields as high as >70% can be achieved with them in unassisted water splitting [3]. However, a rather significant drawback of SrTiO₃ is its wide band gap of 3.2 eV [4], so it can only be excited efficiently with UV photons. Developing visible light active photocatalysts opens up a range of applications, such as air-cleaning, self-cleaning, and antibacterial surfaces by utilizing artificial light indoors. Extending the absorption of SrTiO₃ into the visible region can also benefit outdoor applications in natural solar irradiation, as the visible region of the solar spectrum is ~44% [5]. For this purpose, many approaches have been taken in the literature including doping [6–16], phase junction engineering [17], sensitizing with dyes [18], depositing noble metals on the SrTiO₃ surface [19,20], and preparing

composites/heterojunctions [21–27]. Doping is the intentional introduction of impurities into an intrinsic semiconductor to enhance its properties. Many elements have been utilized to dope alkaline earth metal titanates, including nitrogen [28], carbon [29], copper [10–15], manganese [8], chromium [30], lanthanum [31,32], nickel [32], iron [33], and rhodium [34–42].

It has been shown that doping with Rh is an effective way to enhance the visible light absorption of SrTiO₃ [34,38,39,43–46]. Incorporating Rh into the crystal lattice introduces in-gap impurity levels, raising the valence band maximum without affecting the conduction band minimum level [35], while also changing the character of the semiconductor from n-type to p-type [44]. Most studies showed that during this process, the substitutional replacement of Ti sites to Rh occurs [34–39]. However, the occupancy of alkaline earth metal sites (Sr in this case) by Rh has also been reported in some cases [40–42]. Considering Ti replacement, plausibly, Rh should remain in the Rh⁴⁺ state as it occupies Ti⁴⁺

* Corresponding author.

** Corresponding author at: Department of Applied and Environmental Chemistry, University of Szeged, Rerrich Béla Sqr. 1, Szeged 6720, Hungary

E-mail addresses: gyulavarit@chem.u-szeged.hu (T. Gyulavári), pzsolt@chem.u-szeged.hu (Z. Pap).

<https://doi.org/10.1016/j.cattod.2024.115161>

Received 26 August 2024; Received in revised form 12 November 2024; Accepted 7 December 2024

Available online 11 December 2024

0920-5861/© 2024 The Authors. Published by Elsevier B.V. This is an open access article under the CC BY-NC-ND license (<http://creativecommons.org/licenses/by-nc-nd/4.0/>).

sites. However, Rh has been shown to change its oxidation state [34,35], even during photocatalytic reactions [47]. This is relevant because depending on the Rh oxidation states, photoactivity changes: materials containing Rh⁴⁺ tend to be less photochemically active than those containing only Rh³⁺ [35]. Increasing the number of Rh dopants introduced into the SrTiO₃ lattice also introduces crystal strains, affecting the properties and overall photocatalytic activity of materials, which aspect is poorly investigated.

This study investigates the effect of Rh doping, in as high as 15 at% amounts, on the properties of SrTiO₃ photocatalysts. Aspects such as the Rh oxidation state, complete Rh incorporation versus possible Rh deposition, and the effect of crystal strains are also considered. Since phenol has only been scarcely used to evaluate the photoactivity of Rh-doped SrTiO₃, phenol was selected as a model pollutant and outstanding photoactivity has been achieved in comparison to similar works in the literature.

2. Experimental

2.1. Materials

Sr(OH)₂·8 H₂O (Alfa Aesar, 99.0%), and P25 TiO₂ (Acros Organics, >99.5%) were used as precursors. RhCl₃ (ThermoFisher, 99.95%) was used for doping. Phenol (Spektrum 3D, analytical grade) was used for photocatalytic activity measurements.

2.2. Synthesis

The SrTiO₃ photocatalysts were synthesized following a hydrothermal approach reported by Kiss et al. [34] with slight modifications. The amount of Rh dopant was set to 0, 1, 5, 10, and 15 at%. A detailed description is included in the [supplementary material](#). The samples were named „STO_X_Rh”, where „STO” corresponds to “SrTiO₃” and “X” corresponds to the Rh amount used for doping in at%.

2.3. Characterization methods and instrumentation

X-ray diffraction (XRD) patterns were recorded with a Rigaku Miniflex II diffractometer to investigate crystalline composition using λ_{Cu Kα} = 0.15406 nm radiation (30 mA, 40 kV) in the 2θ–80 (2θ°) region. Average crystallite sizes and crystal strains were calculated using the following equations:

(i) Scherrer equation

$$D = \frac{K \lambda_x}{\beta_{hkl} \cos\theta} \quad (1)$$

(ii) Williamson–Hall (W–H) equation [48]

$$\beta_{hkl} \cos\theta = \frac{K\lambda_x}{D} + 4\varepsilon \sin\theta \quad (2)$$

(iii) Size–strain plot (SSP)

$$(\beta_{hkl} \cos\theta)^2 = \frac{K}{D} (d_{hkl}^2 \beta_{hkl} \cos\theta) + \left(\frac{\varepsilon}{2}\right)^2 \quad (3)$$

where D is the primary crystallite size, K is the shape factor (0.9), λ_x is the wavelength of the X-rays (0.15406 nm), β_{hkl} is the full width at half maximum, θ is the Bragg angle, ε is the crystal strain, and d is the distance between adjacent planes calculated using the Bragg equation (λ = 2d sinθ). Scanning electron microscopy (SEM) and transmission electron microscopy (TEM) images were taken to investigate morphology with Hitachi S-4700 Type II and FEI TECNAI G2 20 X-Twin type microscopes using acceleration voltages of 10 and 200 kV, respectively. Energy-

dispersive X-ray (EDX) analysis was carried out using a Röntec QX2 detector during SEM measurements applying a voltage of 20 kV. Nitrogen adsorption–desorption measurements were carried out to investigate specific surface areas with a NOVA 3000e device, using the Brunauer–Emmett–Teller (BET) method:

$$A_S = n_m a_m N_A \quad (4)$$

where A_S is the specific surface area, n_m is the monomolecular coverage, a_m is the cross-sectional area of the adsorbate (16.2 × 10⁻²⁰ m² per adsorbed nitrogen molecule) and N_A is the Avogadro number (6.022 × 10²³ mol⁻¹). Diffuse reflectance spectroscopy (DRS) measurements were carried out to investigate optical properties with a Jasco-V650 spectrophotometer equipped with an ILV-724-type integration sphere. Band gap energies were calculated and compared using the 1st-order derivative DR spectra [49] and Kubelka–Munk (KM) method (linear fitting on the absorption edge via the Tauc plot after the transformation):

$$F(R_\infty) = \frac{(1 - R_\infty)^2}{2R_\infty} = \frac{K}{S} \quad (5)$$

where R_∞ is the reflectance at infinite thickness, S is the scattering coefficient, and K is the absorption coefficient. Photoluminescence (PL) emission spectra were recorded to investigate exciton recombination with a Horiba Jobin Yvon Fluoromax-4 spectrofluorometer at 350 nm excitation wavelength. Fourier transform infrared (FTIR) spectra were recorded by measuring STO/KBr pellets to investigate functional groups with a Bruker Vertex 70 FTIR instrument between the 400 and 4000 cm⁻¹ range with a resolution of 4 cm⁻¹. X-ray photoelectron spectroscopy (XPS) measurements were carried out to investigate the surface chemical environment with a SPECS PHOIBOS 150 MCD instrument, consisting of a monochromatic Al-Kα source (1486.6 eV), a hemispherical analyzer, and a charge neutralization device. The following parameters were used: 200 W X-ray source, 10⁻⁹–10⁻¹⁰ mbar chamber pressure, calibration of binding energy scale to the C 1 s peak at 284.6 eV, 60 and 20 eV pass energies for recording survey and high-resolution spectra, respectively. Data evaluation was performed in CasaXPS, using a Shirley background and a 70% Gaussian and 30% Lorentzian product form for curve fitting.

2.4. Determination of photocatalytic activity and stability

Phenol (c₀ = 0.1 mM) degradation experiments were carried out to evaluate photocatalytic activity under visible light irradiation. The photocatalyst suspensions were put into a double-walled glass photo-reactor surrounded by six visible-light-emitting fluorescent tubes (Novelite T5, 6 W). The emission spectrum of the lamps is shown in [Fig. S1](#). A blank experiment was also carried out in the absence of phenol to investigate the contribution of photolysis to the conversion values obtained. After adding phenol, the suspensions were stirred in the dark for 10 min to reach adsorption–desorption equilibrium. During the experiments, synthetic air was introduced (Q = 30 L·h⁻¹), the suspension was stirred, and the temperature was maintained at 25 °C. After switching on the lamps, changes in phenol concentrations were followed with a high-performance liquid chromatograph (HPLC), which contained a Merck-Hitachi L-4250 UV-vis detector and a Merck Hitachi L-7100 low-pressure gradient pump. A 50:50 (V/V) methanol/water mixture was used as the eluent, the flow rate was 0.8 mL·min⁻¹, and the detection wavelength was 210 nm.

3. Results and discussion

3.1. Structure, morphology, and optical properties

First, we carried out XRD measurements, and the results are shown in [Fig. 1a](#). The diffraction peaks at 22.9, 32.4, 40.0, 46.4, 52.4, 57.7, 67.7, and 77.1 2θ° can be attributed to the (100), (110), (111), (200), (210),

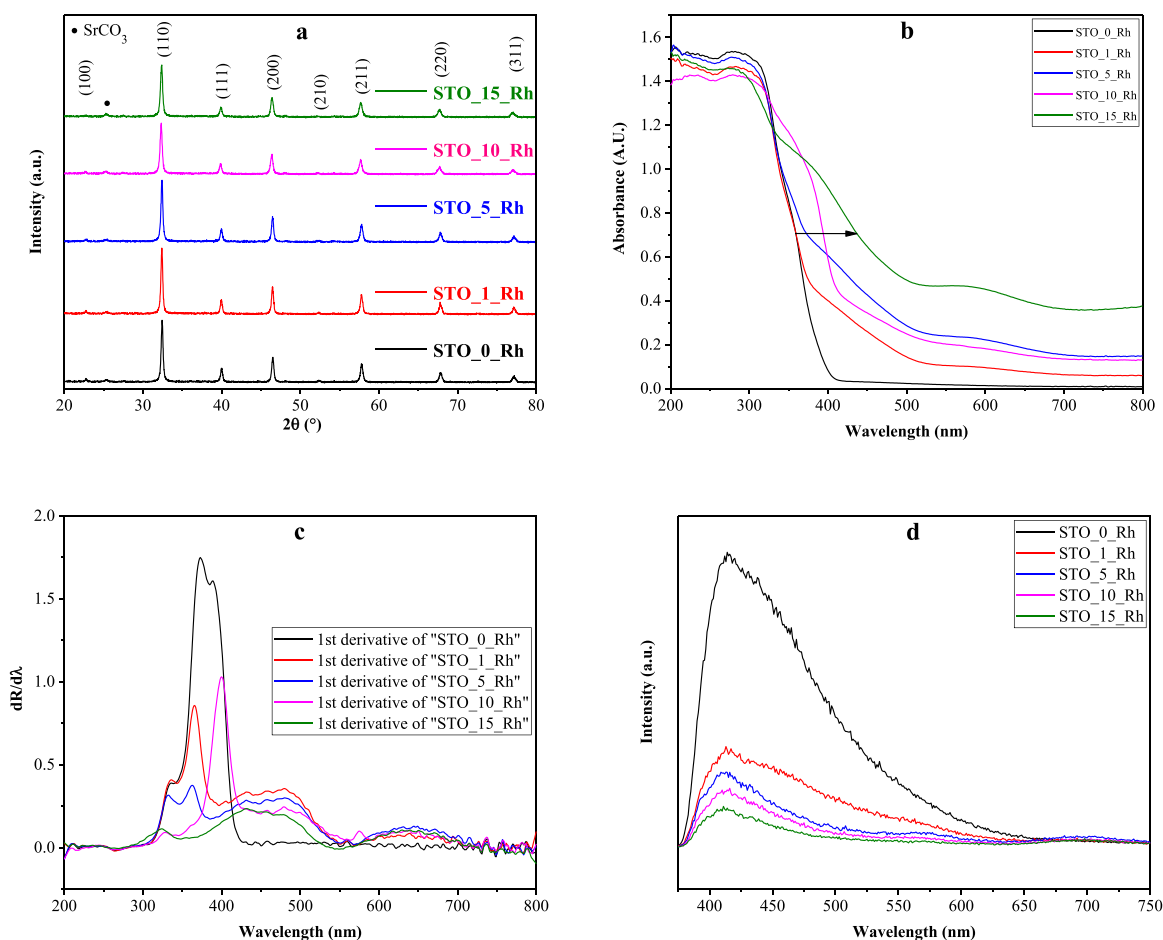


Fig. 1. X-ray diffraction patterns of Rh-doped SrTiO₃ samples (a), their absorbance spectra demonstrating enhanced visible light absorption as a function of increasing Rh amount (b), first-order derivative diffuse reflectance spectra (c), and photoluminescence spectra demonstrating suppressed charge recombination as a function of increasing Rh amount (d).

(211), (220), and (311) crystallographic planes of cubic SrTiO₃, respectively, which agrees with the diffraction data JCPDS 35-0734 [50]. Despite centrifuging the samples with acetic acid at the end of their synthesis, a low amount of SrCO₃ (<2.7%) could also be detected at 25.28 2θ° [4]. We can also observe the diffraction peaks gradually shifting by ~0.15 degrees presumably due to the increasing Rh amount (Fig. S2). This might be because as Rh atoms replace Ti or Sr atoms in the SrTiO₃ crystal lattice [34], the symmetry somewhat changes resulting in a minor shift (the ionic radii of Ti⁴⁺, Sr²⁺, and Rh³⁺/Rh⁴⁺ are 60–74.5, 132, and 80.5/60.5 pm, respectively [36,51]). The area of diffraction peaks did not change as a function of Rh amount; thus, it can be ascertained that the crystallinity of the samples is equal. Inherently, as the number of Sr/Ti lattice points replaced by Rh dopants increases, strains appear in the crystal structure. Taking this into account, primary crystallite sizes can be calculated more reliably using the W–H and SSP equations because they consider the broadening resulting from crystal strains [52]. Accordingly, primary crystallite sizes were calculated using

not only the Scherrer equation but also the W–H and SSP methods, and the results are shown in Table 1 together with the calculated crystal strains. These results support each other rather well. As expected, the sizes obtained from the W–H plot are consistently greater than those from the Scherrer equation; however, the SSP sizes are consistently smaller. Considering the Rh-containing samples, primary crystallite sizes predominantly decrease with increasing Rh amount. This general trend is valid in each case. The decreasing crystallite size can be explained by the different ionic radii of the dopant causing distortion, increasing crystal strain, and hindering crystallization [53]. Moreover, increasing the number of impurities (i.e., dopants in this case) increases the number of nucleation centers, resulting in decreased crystallite sizes [54]. Based on the literature background provided in the introduction section, the similar ionic radii of Rh and Ti make the replacement of the latter by the former probable. This is also supported by the ~0.15° shift towards lower 2θ° values (Fig. S2) and the overall increasing lattice parameters (Table 1) [40,42]. The decrease in 2θ° values can be

Table 1

Average primary crystallite sizes, crystal strain, band gaps, and phenol degradation rate of the investigated samples.

Sample name	Mean crystallite size (nm)			ε	Lattice parameter (Å)	Band gap _{IKM} (eV)	r _{0,phenol} (10 ⁻¹⁰ M s ⁻¹)
	d _{Scherrer}	d _{W-H}	d _{SSP}				
STO_0_Rh	24.2	30.2	21.1	8.76E-03	3.899	3.25	5.3
STO_1_Rh	26.3	26.7	23.7	9.81E-03	3.904	3.25	192.2
STO_5_Rh	25.2	30.9	22.8	8.81E-03	3.903	3.18	368.2
STO_10_Rh	21.6	28.4	20.8	9.98E-03	3.914	2.73	350.1
STO_15_Rh	21.5	24.4	16.0	1.40E-02	3.908	2.41	307.6

attributed to the substitution of a larger cation in the place of a smaller cation [10]. However, based on the decreasing primary crystallite sizes and increasing crystal strains with increasing Rh content, a case can be made also for Rh replacing Sr. It is worth highlighting that one does not exclude the other: Shenoy et al. reported first-principles calculations on the mixed occupancy of Rh in Sr and Ti sites in $\text{Sr}_{1-x/2}\text{Ti}_{1-x/2}\text{Rh}_x\text{O}_3$ materials [40]. Last, we also measured the specific surface area of STO_0_Rh as a reference and obtained $21.3 \text{ m}^2 \text{ g}^{-1}$.

Second, we investigated optical properties via DRS measurements. As mentioned previously, doping with Rh is an efficient way to increase the visible light absorbance of SrTiO_3 [34,38,39,43–46]. This is also what we observed based on the absorbance spectra in Fig. 1b. As a function of Rh amount, the absorption edge gradually undergoes a significant redshift, while absorbance in the visible region increases. Although it is known that the Kubelka–Munk (KM) function is inaccurate for doped materials [55], still, as an approximate calculation, we evaluated the band gap energies this way too (Table 1). Undoped STO_0_Rh has a band gap of 3.25 eV, which agrees with the values reported in the literature [4,34,56]. Following the increasing Rh content in the sample series, the band gaps change from 3.25 eV to as narrow as 2.41 eV. This is in rather good accordance with the publication of Konta et al., who reported that as narrow as 2.3 eV band gap is achievable by doping SrTiO_3 with Rh [6]. Moreover, the shape of the absorption edge is only straight for STO_0_Rh, which implies that multiple electron transition bands are present in the Rh-containing samples. To investigate this aspect better, we considered the first-order derivative of the diffuse reflectance spectra (Fig. 1c). Additionally, based on the publication of Flak et al., the dependence of excitability on the wavelength can also be determined better via this approach [49]. The first-order derivative spectra are rather complex. The main band in STO_0_Rh is centered at 373 nm, which equals a band gap of 3.3 eV, which is in reasonably good accordance with the result obtained using the KM method. In parallel with the decreasing intensity of the SrTiO_3 band, the intensity of the wide band centered at $\sim 645 \text{ nm}$ gradually increases with increasing Rh amount. With the increase of Rh content, two broad bands appear, one starting from $\sim 420 \text{ nm}$ and one negative band centered at $\sim 580 \text{ nm}$, which can be attributed to the presence of Rh^{3+} species [38,45] and Rh d–d transitions [34,38], respectively. Kawasaki et al. attributed these bands to Rh^{4+} and Rh^{3+} in-gap states, respectively [35]. Interestingly, the SrTiO_3 band at 373 nm shifts and its intensity decreases with increasing Rh amount (this band disappears in STO_15_Rh). A possible explanation for the disappearance of the SrTiO_3 signal is the formation of a mixed oxide composition (e.g., SrRhO_3 [57], Sr_2RhO_4 [58], $\text{Sr}_3\text{Rh}_2\text{O}_7$ [59], Sr_4RhO_6 [60]) on the surface of the samples; however, the diffuse reflectance properties of such materials have not been investigated to our knowledge. The fact, that our catalysts were prepared using 2% Sr excess, makes the formation of these mixed oxide compositions probable. For example, Kiss et al., whose synthesis method was used to prepare our samples after minor modifications, reported the formation of rhodium oxides (RhO_2 , Rh_2O_3) and a strontium–rhodium mixed oxide (Sr_4RhO_6) based on XPS and XANES results. The disappearance of the SrTiO_3 signal also makes the evaluation of band gaps based on the first-order derivative spectra unreliable; however, all bands centered at ~ 336 , ~ 373 , and $\sim 388 \text{ nm}$ that appear in the doped samples correspond to SrTiO_3 since they are also present in the undoped sample. The appearance of these mixed oxide species probably also contributes to the visible light absorbance of the doped samples.

Optical properties were also investigated by PL measurements, and the results are shown in Fig. 1d. One main emission band was observed centered at $\sim 414 \text{ nm}$. Charge recombination is the highest in the undoped reference sample (STO_0_Rh), as expected. Charge recombination is increasingly more suppressed with the increase of the Rh amount. The spectral shape is asymmetric because the intensity decrease is smaller in the lower energy region, suggesting the presence of defect sites in the lattice (originating from Rh doping), which can also contribute to recombination. This can be the reason for the appearance

of the flat band centered around 700 nm. It is known that better photocatalytic activity can be expected in samples where recombination is suppressed, as the number of excitons available for photocatalytic processes is higher.

Last, we investigated the morphology of the samples by SEM and TEM measurements, and the micrographs are shown in Fig. S3. The figure shows predominantly cubic and angular particles, and the morphology is largely uniform. The morphology does not change as a function of Rh content. Metallic Rh particles cannot be observed on the surface, not even for the sample containing the highest Rh amount (STO_15_Rh). This means that all Rh used during the synthesis was either successfully incorporated into the crystal lattice or mixed rhodium oxides/strontium–rhodium oxides were formed [34], as implied by our DRS results.

3.2. Surface properties

Surface properties were first investigated by IR measurements and the results are shown in Fig. S4. Based on the spectra, the surface of the samples is rather featureless as only the usual metal–oxygen bonds, surface hydroxyl groups, and adsorbed water bands were observed. Specifically, the bands at ~ 447 and $\sim 625 \text{ cm}^{-1}$ can be attributed to the bending and stretching vibrations of TiO_6 octahedra [61], while the ones ~ 680 and $\sim 560 \text{ cm}^{-1}$ correspond to Ti–O–Ti and Ti–O asymmetric stretching vibrations, respectively [62]. The shoulder at $\sim 745 \text{ cm}^{-1}$ represents Sr–O asymmetric stretching vibrations [62]. Last, the bands at ~ 3400 and $\sim 1630 \text{ cm}^{-1}$ can be ascribed to the stretching and bending vibrations of surface OH/ H_2O groups and surface OH groups, respectively [63,64]. The intensity of these latter two bands increases as a function of Rh amount, indicating that the hydrophilicity of the samples increases, which might influence photoactivity.

The surface of the samples was further studied by XPS measurements. The Sr 2p and Ti 2p spectra showed that Sr and Ti were present in their most frequent states: Sr^{2+} and Ti^{4+} , respectively. The O 1s spectra showed species that are normally present on the surface of SrTiO_3 (i.e., lattice oxygen at 530.1 eV, surface OH group at 531.4 eV, and adsorbed water at 532.1 eV; [65,66]). According to the previous section, we propose that the presence of various $\text{Sr}_x\text{Rh}_y\text{O}_z$ species is probable, even in the sample containing as low as 1 at% Rh. This implies that the surface concentration of Rh should be relatively high in each sample compared to the other metal atoms. This is successfully supported by the results obtained based on the survey XP spectra (Table S1). The Rh ratio increases from 20.5% to 31.0% (considering the metal atoms on the surface) as the applied Rh concentration increases from 1 to 15 at%. This result further corroborates the existence of several $\text{Sr}_x\text{Rh}_y\text{O}_z$ surface species, which is in good agreement with the hypothesis proposed when discussing the first-order derivative DR spectra.

As no Rh nanoparticles are present on the surface of the SrTiO_3 crystallites, doping certainly occurs (reinforced also by the XRD patterns and color changes observed in the DR spectra), as shown in Fig. 2. The Rh 3d XP spectra identified two Rh species: Rh^{3+} (at 308.1 and 312.9 eV, corresponding to the $3d_{5/2}$ $3d_{3/2}$ orbitals, respectively) and Rh^{4+} (at 309.7 and 314.8 eV, corresponding to the $3d_{5/2}$ and $3d_{3/2}$ orbitals, respectively), while no metallic Rh (at 307.5 and 311.6 eV) was observed [34,67]. The ratio of these two species is shown in Table S1. The Rh 3d spectrum of STO_1_Rh was unsuitable for deconvolution, due to the high noise/signal ratio (integration was executed only to estimate concentrations), hence it was omitted from this discussion (Fig. S5). As more Rh is added as the dopant, the concentration of Rh^{3+} decreases, while Rh^{4+} increases (Table S1, Fig. 2): in STO_5_Rh, Rh^{3+} is present in 26.1%, which decreases to 5.8% in STO_15_Rh. The ratio of these species may affect the overall photoactivity of the samples as shown by similar works in the field [34].

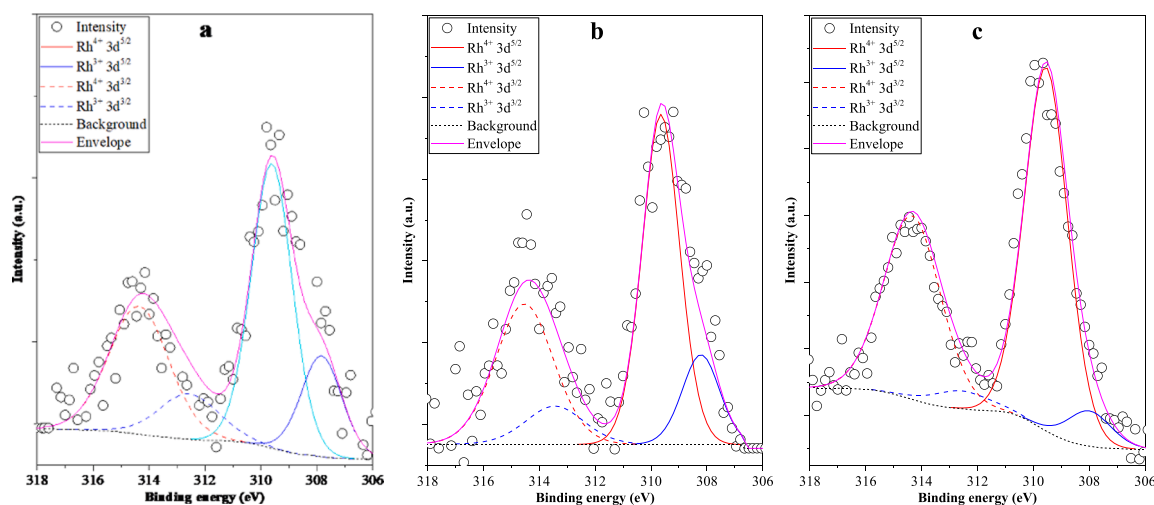


Fig. 2. X-ray photoelectron Rh 3d spectra of the investigated samples: a) STO_5_Rh, b) STO_10_Rh, and c) STO_15_Rh.

3.3. Photocatalytic activity

The photocatalytic activity of the samples was evaluated via the degradation of phenol under visible light irradiation. First, the photocatalysts were stirred in the dark for 5 min to establish an adsorption–desorption equilibrium. Based on Fig. 3, the degree of adsorption was between 2% and 6% in all cases, which can be because phenol is known to be a poorly adsorbing compound. The STO_0_Rh reference only degraded ~10% phenol over the course of 4 h. However, after doping with only 1 at% Rh, the conversion increased from ~10% to ~90%. The calculated reaction rates are included in Table 1. The best-performing sample is STO_5_Rh, which degraded ~99% phenol in 1 h. Past this threshold, further increasing the Rh amount did not lead to a further increase in photocatalytic activity; on the contrary, photoactivity gradually decreased with the increase of Rh incorporated into the crystal lattice. A possible explanation is that materials containing more Rh³⁺ and less Rh⁴⁺ tend to be more photochemically active [35]. This statement is also supported by the results of Kiss et al., who reported that Rh⁴⁺ can act as recombination sites for photogenerated excitons resulting in lower photoactivity [34]. Our XPS results also confirm this hypothesis. Regarding the degradation mechanism, it is known that the

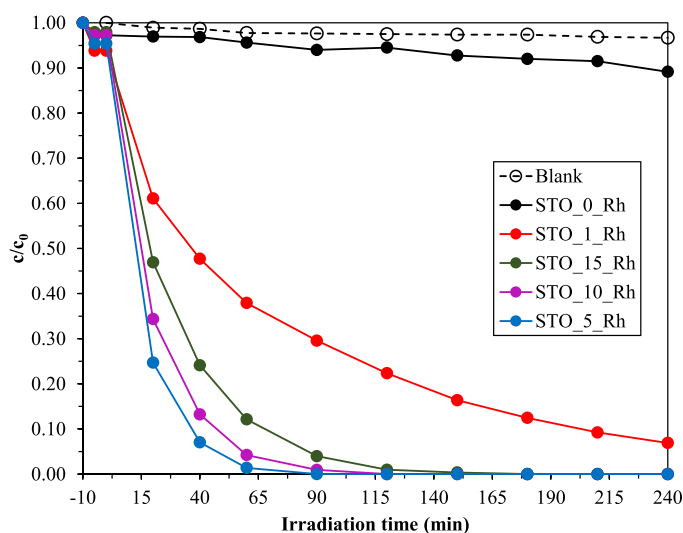


Fig. 3. Photocatalytic degradation curves of phenol carried out under visible light irradiation ($c_{0,phenol} = 0.1$ mM; $c_{photocatalyst} = 1$ g L⁻¹; $\lambda > 400$ nm).

ability of photogenerated holes to produce hydroxyl radicals is lower under visible light than under UV light [68]. However, during the photocatalytic oxidation of phenol, hydroxylated byproducts (i.e., hydroquinone and pyrocatechol) were formed (Fig. S6), demonstrating that degradation occurred via hydroxyl radicals.

The phenol degradation efficiency of our best sample (STO_5_Rh) was also compared with that of other SrTiO₃-based photocatalysts reported in the literature [24,29,69–75]. For this purpose, the best-performing sample was selected from each work, and publications using visible light irradiation were considered. The comparison is shown in Table 2. Based on the table, our STO_5_Rh sample is among the best photocatalysts, especially considering that the light source we used (visible-light-emitting fluorescent tubes) requires the lowest amount of energy (6 × 6 W) to operate.

4. Conclusions

A series of Rh-doped SrTiO₃ photocatalysts were successfully synthesized. XRD and TEM results demonstrated that all the Rh applied during synthesis was incorporated into the crystal lattice. Primary crystallite sizes obtained via the Scherrer, W–H, and SSP equations showed that the sizes decreased with increasing Rh amount, which was attributed to crystal strains originating from Rh replacing Ti or Sr in the crystal lattice. DRS results demonstrated enhanced visible light absorbance (from 3.25 to 2.41 eV), while PL results indicated suppressed charge recombination due to Rh doping. The formation of mixed oxide species on the surface of the samples was presumed to contribute to the enhanced visible light absorbance. The optimal rhodium amount resulting in the highest photoactivity gain under visible light irradiation was 5 at%. The phenol degradation performance of the photocatalysts was increased to an exceptionally high degree from 5.3 to 368.2×10^{-10} M s⁻¹, which is among the best photocatalysts reported in the literature.

CRedit authorship contribution statement

Áron Ágoston: Writing – original draft, Visualization, Investigation. **Ákos Kukovecz:** Resources, Methodology, Funding acquisition. **Fanni Bóka:** Visualization, Validation, Investigation. **Milica Todea:** Writing – original draft, Visualization, Investigation. **Tamás Gyulavári:** Writing – review & editing, Writing – original draft, Visualization, Supervision, Investigation, Funding acquisition, Conceptualization. **Zsolt Pap:** Writing – review & editing, Visualization, Supervision, Funding acquisition, Conceptualization. **Zoltán Kónya:** Visualization, Supervision, Conceptualization.

Table 2

Comparison of phenol degradation efficiencies of different SrTiO₃-based photocatalysts in the literature with that reported in this study.

Photocatalyst	Photocatalyst concentration (g/L)	Phenol degradation (%)	Degradation time (min)	Phenol concentration (mM)	Light source	Reference
SrTiO ₃ /SrMoO ₄	1	~80	90	0.5	Visible LED (46.1 W/m ²)	[69]
C-SrTiO ₃	–	~75	180	0.1	Xenon lamp (500 W)	[29]
AgPO ₄ /PANI/Cr-SrTiO ₃	0.5	100	7	0.26	Xenon lamp (300 W)	[70]
Ag-S-SrTiO ₃	–	96 (4-CP)	120	–	Solar	[71]
Pt/SrTiO ₃ -Rh	0.83	~60	360	0.21	Xenon lamp (300 W)	[72]
TiO ₂ /SrTiO ₃ -BiOI	–	~30	60	0.21	Xenon lamp (1000 W)	[73]
3DOM-SrTiO ₃ /Ag/Ag ₃ PO ₄	1	100	16	0.106	Xenon lamp (300 W)	[74]
Rh-SrTiO ₃	–	~35	60	0.21	Xenon lamp (1000 W)	[75]
Ag/AgCl/SrTiO ₃	0.5	70	240	0.106	Xenon lamp (300 W)	[24]
Rh-SrTiO ₃	1	~99	60	0.1	Fluorescent tubes (6 × 6 W)	This study

Declaration of Competing Interest

The authors declare that they have no known competing financial interests or personal relationships that could have appeared to influence the work reported in this paper.

Acknowledgements

This study was financed by the NKFI-PD-138248 project. The authors are grateful for the financial support of the 2019–2.1.13-TÉT_IN-2020–00015 and 2021–1.2.6-TÉT-IPARI-MA-2022–00009 projects. T. Gyulavári acknowledges the Bolyai János scholarship (BO/00447/23) provided by the Hungarian Academy of Sciences. This research was supported by the ÚNKP-23–4-SZTE-638 New National Excellence Program of the Ministry for Culture and Innovation from the source of the National Research, Development and Innovation Fund. Áron Ágoston acknowledges the Doctoral Student Scholarship Program of the Co-operative Doctoral Program (EKÖP-KDP-24-SZTE-6) of the Ministry of Innovation and Technology financed from the National Research, Development and Innovation Fund. Project no. TKP2021-NVA-19 has been implemented with the support provided by the Ministry of Innovation and Technology of Hungary from the National Research, Development and Innovation Fund, financed under the TKP2021-NVA funding scheme.

Appendix A. Supporting information

Supplementary data associated with this article can be found in the online version at [doi:10.1016/j.cattod.2024.115161](https://doi.org/10.1016/j.cattod.2024.115161).

Data availability

Data will be made available on request.

References

- N. Sharma, K. Hernadi, *Catalysts* 12 (2022) 1619.
- S. Patial, V. Hasija, P. Raizada, P. Singh, A.A.P. Khan Singh, A.M. Asiri, *J. Environ. Chem. Eng.* 8 (2020) 103791.
- Z. Zhao, R.V. Goncalves, S.K. Barman, E.J. Willard, E. Byle, R. Perry, Z. Wu, M. N. Huda, A.J. Moulé, F.E. Osterloh, *Energy Environ. Sci.* 12 (2019) 1385–1395.
- B. Boga, N. Steinfeldt, N.G. Moustakas, T. Peppel, H. Lund, J. Rabeah, Z. Pap, V.-M. Cristea, J. Strunk, *Catalysts* 12 (2022) 978.
- D.M. Schultz, T.P. Yoon, *Science* 343 (2014) 1239176.
- R. Konta, T. Ishii, H. Kato, A. Kudo, *Chem. Inform.* 35 (2004).
- J. Xu, Y. Wei, Y. Huang, J. Wang, X. Zheng, Z. Sun, L. Fan, J. Wu, *Ceram. Int.* 40 (2014) 10583–10591.
- G. Wu, P. Li, D. Xu, B. Luo, Y. Hong, W. Shi, C. Liu, *Appl. Surf. Sci.* 333 (2015) 39–47.
- J. Zhu, Y. Zhang, L. Shen, J. Li, L. Li, F. Zhang, Y. Zhang, *Powder Technol.* 410 (2022) 117886.
- D.K. Bhat, U. Pi, U.S. Shenoy, *J. Hazard. Mater. Adv.* 12 (2023) 100380.
- U. P. I, U.S. Shenoy, D.K. Bhat, *ACS Appl. Nano Mater.* 6 (2023) 16798–16804.
- D.K. Bhat, P.I. Uma, U.S. Shenoy, *J. Alloy. Compd. Commun.* 4 (2024) 100030.
- U.S. Shenoy, P.I. Uma, D.K. Bhat, *J. Alloy. Compd.* 1004 (2024) 175779.
- P.I. Uma, U.S. Shenoy, D.K. Bhat, *J. Alloy. Compd.* 948 (2023) 169600.
- P.I. Uma, U.S. Shenoy, D.K. Bhat, *Appl. Surf. Sci. Adv.* 15 (2023) 100408.
- A. Bhava, U.S. Shenoy, D.K. Bhat, *Environ. Pollut.* 344 (2024) 123430.
- A.K. Singh, S.K. Pandey, P.K. Vishwakarma, R. Pratap, R. Verma, A. Pandey, R. Giri, A. Srivastava, *Oxf. Open Mater. Sci.* 3 (2023).
- P. Jayabal, V. Sasirekha, J. Mayandi, K. Jeganathan, V. Ramakrishnan, *J. Alloy. Compd.* 586 (2014) 456–461.
- M. Yadav, T. Gyulavári, J. Kiss, K.B. Ábrahám, A. Efreanova, Á. Szamosvölgyi, Z. Pap, A. Sági, Á. Kukovecz, Z. Kónya, *J. CO₂ Util.* 78 (2023) 102621.
- P.F. Lim, K.H. Leong, L.C. Sim, W.-D. Oh, Y.H. Chin, P. Saravanan, C. Dai, *Appl. Phys. A* 126 (2020).
- G. Wu, L. Xiao, W. Gu, W. Shi, D. Jiang, C. Liu, *RSC Adv.* 6 (2016) 19878–19886.
- T. Kanagaraj, S. Thiripuranthagan, *Appl. Catal. B Environ.* 207 (2017) 218–232.
- Q. Jia, A. Iwase, A. Kudo, *Chem. Sci.* 5 (2014) 1513.
- S.-F. Yang, C.-G. Niu, D.-W. Huang, H. Zhang, C. Liang, G.-M. Zeng, *Environ. Sci. Nano* 4 (2017) 585–595.
- T. Xie, X. Ma, Q. Li, X. Tian, J. Si, *J. Solid State Chem.* 337 (2024) 124793.
- D.K. Bhat, H. Bantawal, U. P.I, U.S. Shenoy, *Diam. Relat. Mater.* 139 (2023) 110312.
- D.K. Bhat, H. Bantawal, P.I. Uma, S.P. Kumar, U.S. Shenoy, *Sustain. Chem. Environ.* 5 (2024) 100071.
- I. Atkinson, V. Parvulescu, J. Pandele Cusu, E.M. Anghel, M. Voicescu, D. Culita, S. Somacescu, C. Munteanu, M. Săcepanović, Z.V. Popovic, V. Fruth, *J. Photochem. Photobiol. A Chem.* 368 (2019) 41–51.
- C.-W. Chang, C. Hu, *Chem. Eng. J.* 383 (2020) 123116.
- F. Cai, Y. Tang, F. Chen, Y. Yan, W. Shi, *RSC Adv.* 5 (2015) 21290–21296.
- D. Yang, X. Zou, Y. Sun, Z. Tong, Z. Jiang, *Front. Chem. Sci. Eng.* 12 (2018) 440–449.
- A. Jia, X. Liang, Z. Su, T. Zhu, S. Liu, *J. Hazard. Mater.* 178 (2010) 233–242.
- T.-H. Xie, X. Sun, J. Lin, *J. Phys. Chem. C* 112 (2008) 9753–9759.
- B. Kiss, T.D. Manning, D. Hesp, C. Didier, A. Taylor, D.M. Pickup, A.V. Chadwick, H.E. Allison, V.R. Dhanak, J.B. Claridge, J.R. Darwent, M.J. Rosseinsky, *Appl. Catal. B Environ.* 206 (2017) 547–555.
- S. Kawasaki, K. Nakatsuji, J. Yoshinobu, F. Komori, R. Takahashi, M. Lippmaa, K. Mase, A. Kudo, *Appl. Phys. Lett.* 101 (2012).
- P. Shen, J.C. Lofaro, W.R. Woerner, M.G. White, D. Su, A. Orlov, *Chem. Eng. J.* 223 (2013) 200–208.
- M. Antuch, P. Millet, A. Iwase, A. Kudo, *Electrochim. Acta* 297 (2019) 696–704.
- T. Baran, *React. Kinet. Mech. Catal.* 136 (2023) 3243–3256.
- S. Hara, M. Yoshimizu, S. Tanigawa, L. Ni, B. Ohtani, H. Irie, *J. Phys. Chem. C* 116 (2012) 17458–17463.
- U.S. Shenoy, H. Bantawal, D.K. Bhat, *J. Phys. Chem. C* 122 (2018) 27567–27574.
- U.S. Shenoy, D.K. Bhat, *J. Phys. Chem. Solids* 148 (2021) 109708.
- D.K. Bhat, H. Bantawal, U.S. Shenoy, *Nanoscale Adv.* 2 (2020) 5688–5698.
- H. Kato, Y. Sasaki, N. Shirakura, A. Kudo, *J. Mater. Chem. A* 1 (2013) 12327.
- K. Iwashina, A. Kudo, *J. Am. Chem. Soc.* 133 (2011) 13272–13275.
- Y. Kuo, K.J. Klabunde, *Nanotechnol.* 23 (2012) 294001.
- J.Q. Su, Y.-C. Chang, J.C.S. Wu, *Catalysts* 11 (2021) 383.
- T. Shinoda, Y. Yamaguchi, A. Kudo, N. Murakami, *Chem. Commun. Camb.* 56 (2020) 14255–14258.
- G. Panomsuan, H. Manuspiya, *Ferroelectrics* 554 (2020) 30–37.
- D. Flak, A. Braun, B.S. Mun, J.B. Park, M. Parlinska-Wojtan, T. Graule, M. Rekas, *Phys. Chem. Chem. Phys.* 15 (2013) 1417–1430.
- M.-V. Le, N.-Q.-D. Vo, Q.-C. Le, V.A. Tran, T.-Q.-P. Phan, C.-W. Huang, V.-H. Nguyen, *Catalysts* 11 (2021) 564.
- R.D. Shannon, *Acta Crystallogr. A* 32 (1976) 751–767.
- Z. Kovács, V. Márta, T. Gyulavári, Á. Ágoston, L. Baia, Z. Pap, K. Hernadi, *J. Environ. Chem. Eng.* 10 (2022) 107655.
- F. Ben Jemaa, S. Mahmood, M. Ellouze, E.K. Hlil, F. Halouani, *J. Mater. Sci.* 50 (2014) 620–633.

- [54] R. Prasad, P.S. Walke, S.D. Bham, *Mater. Res. Exp.* 6 (2019) 1150b1158.
- [55] P. Makula, M. Pacia, W. Macyk, *J. Phys. Chem. Lett.* 9 (2018) 6814–6817.
- [56] M. Abedi, A. Szamosvölgyi, A. Sági, A. Kukovecz, Z. Kónya, T. Gyulavári, *Z. Pap. Catalysts* 13 (2023) 219.
- [57] A.M. Shawahni, M.S. Abu-Jafar, R.T. Jaradat, T. Ouahrani, R. Khenata, A. A. Mousa, K.F. Ilaiwi, *Materials* 11 (2018).
- [58] L.J. Sandilands, W. Kyung, S.Y. Kim, J. Son, J. Kwon, T.D. Kang, Y. Yoshida, S. J. Moon, C. Kim, T.W. Noh, *Phys. Rev. Lett.* 119 (2017) 267402.
- [59] K. Yamaura, Q. Huang, D.P. Young, Y. Noguchi, E. Takayama-Muromachi, *Phys. Rev. B* 66 (2002).
- [60] A. Banerjee, R. Prasad, V. Venugopal, *J. Alloy. Compd.* 381 (2004) 58–62.
- [61] T. Xian, H. Yang, L. Di, J. Ma, H. Zhang, J. Dai, *Nanoscale Res. Lett.* 9 (2014) 327.
- [62] J.H. Roque-Ruiz, J. Meraz-Angel, R. Farias, M. Melendez-Lira, S.Y. Reyes-Lopez, *J. Ceram. Sci. Technol.* 10 (2019) 29–37.
- [63] J. Orlikowski, B. Tryba, J. Ziebro, A.W. Morawski, J. Przepiórski, *Catal. Commun.* 24 (2012) 5–10.
- [64] X. Ye, C. Zheng, L. Ma, X. Huang, *Mater. Sci. Semicond. Process.* 31 (2015) 295–301.
- [65] R.P. Vasquez, *Surf. Sci. Spectra* 1 (1992) 129–135.
- [66] T. Suwannaruang, P. Kidkhunthod, T. Butburee, H.P. Shivaraju, B. Shahmoradi, K. Wantala, *Surf. Interfaces* 23 (2021) 101013.
- [67] Y. Abe, K. Kato, M. Kawamura, K. Sasaki, *Surf. Sci. Spectra* 8 (2001) 117–125.
- [68] A.M. Abdullah, M.A. Gracia-Pinilla, S.C. Pillai, K. O'Shea, *Molecules* 24 (2019).
- [69] P. Basumatary, S. Saha, A. Ramchiary, D. Konwar, *J. Phys. Chem. Solids* 188 (2024) 111939.
- [70] X. Yu, Y. Lin, H. Liu, C. Yang, Y. Peng, C. Du, S. Wu, X. Li, Y. Zhong, *J. Colloid Interface Sci.* 561 (2020) 379–395.
- [71] B.G. Anitha, L.G. Devi, *Surf. Interfaces* 16 (2019) 50–58.
- [72] D. Li, J.C.-C. Yu, V.-H. Nguyen, J.C.S. Wu, X. Wang, *Appl. Catal. B Environ.* 239 (2018) 268–279.
- [73] M. Marchelek, E. Grabowska, T. Klimczuk, W. Lisowski, P. Mazierski, A. Zaleska-Medynska, *Mol. Catal.* 452 (2018) 154–166.
- [74] C. Zhang, K. Yu, Y. Feng, Y. Chang, T. Yang, Y. Xuan, D. Lei, L.-L. Lou, S. Liu, *Appl. Catal. B Environ.* 210 (2017) 77–87.
- [75] E. Grabowska, M. Marchelek, T. Klimczuk, W. Lisowski, A. Zaleska-Medynska, *J. Catal.* 350 (2017) 159–173.